Phonon protected superconducting qubit

Mutasem Odeh,[1,2] Kadircan Godeneli,[1,2] Eric Li,[1] Rohin Tangirala,[1] Zihuai Zhang,[1,2] Haoxin Zhou,[1,2] Xueyue Zhang,[1,2] and Alp Sipahigil[1,2,3,*]

[1]*Department of Electrical Engineering and Computer Sciences, University of California, Berkeley, Berkeley, California 94720, USA*

[2]*Materials Sciences Division, Lawrence Berkeley National Laboratory, Berkeley, California 94720, USA*

[3]*Department of Physics, University of California, Berkeley, Berkeley, California 94720, USA*

(Dated: October 3, 2023)

The overhead of physical qubits required to build a logical qubit scales rapidly with the qubit decoherence rate, whereas the latter scales inversely with the qubit footprint due to the unavoidable interaction with the two-level system (TLS) environment. The two scalings jointly pose a hard limit on the realization of integrated fault-tolerant quantum processors with practical utility or quantum advantage. In this work, we utilize an engineered phononic crystal as a mechanical Purcell filter to shield a transmon qubit from indirect phonon emissions mediated by TLSs. We observe a significant improvement in TLS relaxation time, increasing from a few hundred nanoseconds to an average of $34\,\mu$s inside the phononic bandgap. Despite the compact qubit geometry and the high density of TLSs of the fabricated device, we observe a noticeable enhancement in the qubit's coherence. Our results show that the phonon-shielding efficacy improves in principle as the qubit is miniaturized, paving a path for a promising generation of qubits that scale well for future quantum applications.

A quantum processor with practical utility requires a large number of highly-coherent physical qubits in order to apply error correction and mitigation schemes [1–3]. While many physical qubits have met the coherence threshold criteria [4, 5], it has come at the expense of the qubit footprint, which hinders practical scaling considering the qubit overhead required. Moreover, large-scale quantum algorithms, such as Shor's factoring [6] and Grover's search [7], will require thousands of fault-tolerant logical qubits to achieve a real quantum advantage [8].

Miniaturizing qubits while simultaneously maintaining their coherence is a challenging task, as it is fundamentally opposed by the decoherence of tunneling two-level systems (TLSs). TLSs are commonly understood to be surface or bulk defects within disordered or amorphous solids. They commonly have coupled electric and elastic dipole moments, rendering them the major decoherence source of modern superconducting qubits [9–11]. Using large and planar qubit geometry is the common approach to mitigate TLS loss. Despite the short-term gain of this tactic, qubit coherence has plateaued at a few hundred microseconds over the last decade, with a qubit footprint that is impractical for future scaling [12–15].

In this work, we propose a new strategy that, in principle, addresses the coherence-footprint trade-off by incorporating a degree of phonon protection into the hardware itself. Starting from the current understanding of TLS as an atomic-sized piezoelectric transducer, we use a phononic bandgap metamaterial to suppress the TLS phononic spontaneous emission, which, in turn, influences the measured qubit lifetime through a Purcell-effect argument. We characterize a dense bath of weakly coupled TLSs through a series of saturation pulses [16, 17] and perform spectroscopy across the phononic bandgap edge to observe a clear signature of TLS and qubit lifetime enhancement. The observations are well-modeled with the recently developed Solomon equations [18, 19], and the platform opens a path for studying complicated non-Markovian dynamics and correlated errors in superconducting devices [20–22]. We coin this class of qubits as 'phonon-protected' and show, in principle, that the noise protection strategy is more effective with qubit miniaturization, a promising path for scalable qubits in future quantum processors.

Phonon-protected superconducting transmon. According to the standard tunneling model, the principal origin of TLS dissipation can be traced back to their asymmetric energy configuration, which renders them as atomic-size piezoelectric transducers with coupled electric and elastic dipole moments [9]. As illustrated in Fig. 1(b), a TLS resonantly absorbs energy from the oscillating electric field of the qubit and dissipates it to the lattice via phonon emission at a rate Γ_t. Consequently, the qubit will experience a Purcell decay through the TLS with a cross-relaxation rate Γ_{qt}. The total qubit decay rate is then the sum of its intrinsic decay rate Γ_q and the cross-relaxation rates of all coupled TLSs:

$$\Gamma_1 = \Gamma_q + \sum_k \frac{2g_k^2\Gamma_2}{\Gamma_2^2 + \Delta_k^2} \tag{1}$$

where Δ_k represents the detuning between the qubit and the kth TLS, g_k is their transverse coupling strength, and $\Gamma_2 = \Gamma_2^q + \Gamma_2^{t,k}$ is the mutual decoherence, with $\Gamma_2 = \Gamma_1/2$ in the absence of dephasing. For a countable number of TLSs, the coherences of the qubit and TLSs are linked. The latter can be improved by using a phononic crystal (PhC) that suppresses the density of phonon states, resulting in a reduction of TLS decay Γ_t, and consequently the qubit decay Γ_q [23]. Therefore, a phononic crystal

* Corresponding author: alp@berkeley.edu

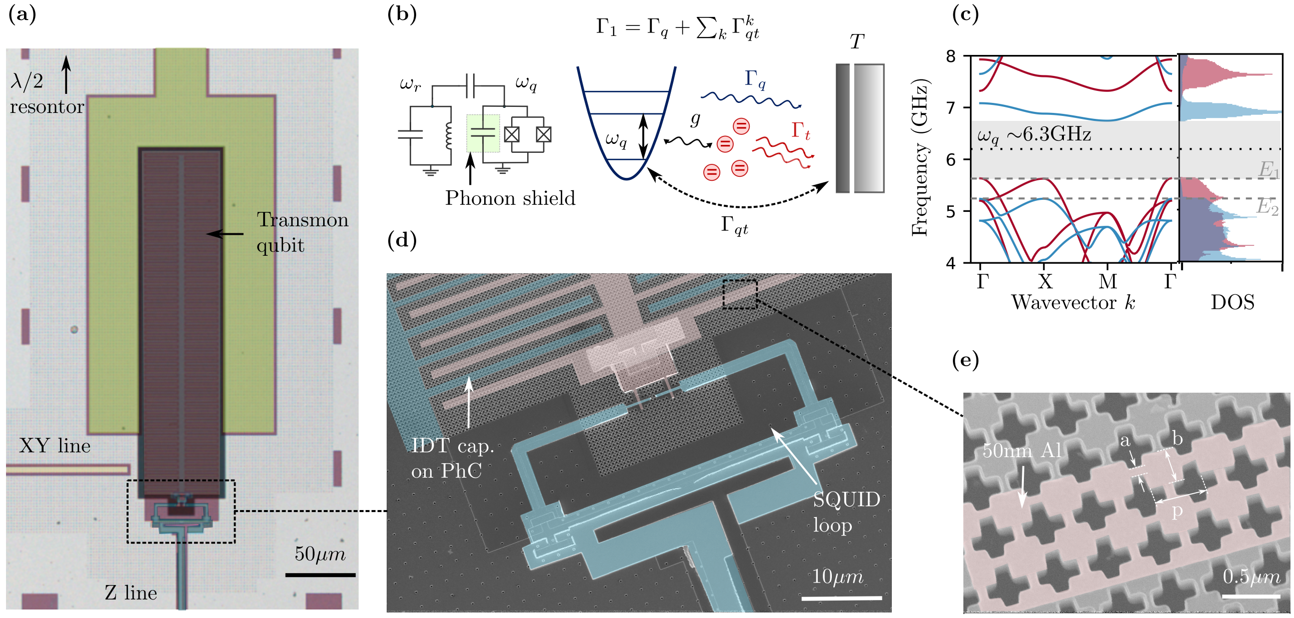

FIG. 1. **Phonon-protected superconducting transmon.** (a) Optical micrograph (false-colored) of the fabricated transmon qubit, formed by an interdigitated capacitor (IDC) and a pair of Josephson junctions (JJ) on a released silicon-on-insulator (SOI) substrate. The qubit is capacitively coupled to a half-wave coplanar waveguide resonator for readout (green), to an XY line for control (yellow), and inductively coupled to a Z-line for frequency tuning (blue). (b) Schematic showing the device circuit formed by a readout resonator coupled to a phonon-shielded transmon with frequencies ω_r and ω_q, respectively. The qubit and two-level systems (TLSs) defects have direct relaxation rates of Γ_q and Γ_t to the environment, respectively, and an cross-relaxation rate of Γ_{qt} mediated by a qubit-TLS coupling strength g. (c) Simulated acoustic band structure of the realized phononic crystal alongside the projected density of states (DOS). The energy bands of 190 nm-thick Si unit cell has a bottom bandgap edge E_1 =5.6 GHz (red) where the bands for 220/50nm-thick Si/Al unit cell has a bottom edge E_2=5.2 GHz (blue). The common acoustic bandgap is highlighted in gray, and the dashed line indicates the maximum transmon frequency $\omega_q/2\pi \approx$6.3 GHz. (d) False-colored scanning electron microscope (SEM) image of the interdigitated capacitor arms (pink, blue), each with a width and spacing of 1 μm, both modulated by the underlying etched phononic crystal. (e) False-colored SEM image of one of the IDT capacitor arms, displaying the PhC shield. The measured unit cell parameters are a = 70 nm, b = 320 nm, and p = 445 nm.

can be thought of as a mechanical Purcell filter.

Our circuit consists of an all-aluminum tunable transmon on a suspended 2D phononic crystal membrane (Fig. 1(a)). The transmon qubit consists of a compact interdigitated capacitor (IDC) shunted to the ground through a symmetric Josephson junction pair that forms a superconducting quantum interference device (SQUID), as shown in Fig. 1(b). The SQUID loop is inductively coupled to a DC control line, allowing the qubit frequency to be tuned over the PhC bandgap edge (5.2 GHz). The transmon is also capacitively coupled to an XY line for qubit control and to a $\lambda/2$ coplanar waveguide resonator for fast dispersive readout. The device is mounted at the mixing chamber stage (∼10 mK) of a dry dilution refrigerator and enclosed in multilayer radiation and magnetic shields. Details about the fabrication process, experimental setup, and measured qubit parameters are provided in [24].

The qubit capacitor is formed by interdigitating 1 μm-wide arms with 1 μm spacing. The entire IDC is fully engraved by the underlying phononic crystal structure, as shown in Fig. 1(e). The challenge of simulating the 260 µm × 60 µm capacitor with 50 nm features was addressed by resorting to the effective medium representation of the PhC, a technical discussion that is provided in [24]. The presence of aluminum loading alters the band structure and shifts the bottom band edge from 5.6 GHz to 5.2 GHz (Fig. 1(c)), a signature that will be visible in subsequent qubit measurements. The common bandgap is centered at 6.2 GHz and spans a 1.2 GHz frequency range. At $\omega_q/2\pi$ =6.3 GHz, we measure a T_1 coherence time of 0.42 µs and Ramsey dephasing T_2^* of 0.61 µs. The qubit can be tuned continuously from 4–6.3 GHz with no signatures of swapping or splitting, suggesting an incoherent interaction with the TLS environment. The transmon's designed and measured parameters, along with coherence characterization, can be found in [24].

Polarization of TLS bath. When the coupling strength of a TLS that is on-resonance with a qubit is greater than their mutual decoherence rate ($g_k > \Gamma_2^k$), coherent oscillations are observed, from which swap spectroscopy can be used to calculate the TLS lifetime [25].

As the mutual decoherence increases ($g_k < \Gamma_2^k$), the qubit and TLS populations follow the Solomon rate equations [19]:

$$\dot{p}_q = -\Gamma_q(p_q - p_{th}) - \sum_k \Gamma_{qt}^k(p_q - p_t^k) \tag{2}$$

$$\dot{p}_t = -\Gamma_t(p_t^k - p_{th}) - \Gamma_{qt}^k(p_t^k - p_q) \tag{3}$$

with p_q, p_t, p_{th} referring to the qubit, TLS, and thermal populations, respectively. In this regime, the TLS lifetime can be measured by first polarizing the TLS bath and then inferring its properties from the qubit dynamics. The pulse sequence is shown in Fig. 2(a) and consists of X_π pulses that prepare the qubit in the $|e\rangle$ state at a reference frequency ω_0. The excitation is subsequently exchanged with the TLS environment at ω_q by simply letting the qubit relax ($\tau_r > 1/\Gamma_1$). The sequence is repeated N times, after which a free decay measurement is carried out by first initializing the qubit to either $|g\rangle$ or $|e\rangle$ state, holding the qubit for τ_d at the polarized bath frequency ω_q, and then a qubit readout at the reference frequency ω_0.

The qubit population approximately represents the TLS population ($p_q \approx p_t$) when it is allowed to reach equilibrium by setting $\tau_d \gg 1/\Gamma_1$. Fig. 3(b) shows the TLS population as a function of the number of polarization pulses N. Around $N = 200$, the TLS bath can be populated from its thermal state$p_{th} \approx 6\%$ to around $p_{eq} \approx 30\%$ around the center of the phononic bandgap (∼6.28 GHz), pointing to the presence of long-lived TLSs. This is in stark contrast to frequencies outside the bandgap (∼4.5 GHz), where the TLS can't be populated due to their very short lifetime (∼100 ns).

A spectral scan of the populated TLS bath (Fig. 2(c)) can be fitted to a Lorentzian with a linewidth of approximately ∼6 MHz. This indicates that the populated TLSs are dense and share similar cross-relaxation rates. As seen in Fig. 2(d), interleaved polarization pulses can also be used to saturate the dense bath at different spectral regions, thereby allowing the study of complex non-Markovian dynamics. Under the dense bath approximation ($\Gamma_{qt}^k \approx \Gamma_{qt}$), the Solomon rate equations can be simplified to [19, 24]:

$$\dot{p}_q = -\Gamma_1(p_q - p_{th}) + \Gamma_{TLS} p_{t,0}^* e^{-\Gamma_t t} \tag{4}$$

In the case of long-lived TLSs ($\Gamma_t \ll \Gamma_1$), the solution to the above differential equation can be approximated by the biexponential $p_q(t) \approx a e^{-\Gamma_1 t} + b e^{-\Gamma_t t} + p_{th}$, as detailed in [24]. Figure 2(e) illustrates the qubit decay after $N = 200$ polarization pulses with the qubit initialized in the $|g\rangle$ and $|e\rangle$ states. From the curves-fitting, we observe that, on average, the qubit lifetime $1/\Gamma_1 \approx 0.58\,\mu$s is independent of the TLS population and the TLS lifetime $1/\Gamma_t \approx 35.5\,\mu$s is independent of the qubit initialization.

Phononic bandgap spectrsocpy. To study the influence of the phononic bandgap, we performed the polarization pulse sequence depicted in Fig. 2(a) over the frequency range of 4–6.25 GHz, with a time delay of up to τ_d =250 µs, capturing both slow and fast qubit dynamics. The results are presented in Fig. 3(a), revealing a sudden suppression of long-term qubit population outside the bandgap. The data were fitted to the biexponential solution $p_q(t) \approx a e^{-\Gamma_1 t} + b e^{-\Gamma_t t} + p_{th}$ to extract the TLS ($1/\Gamma_t$) and qubit ($1/\Gamma_1$) lifetimes, as shown in

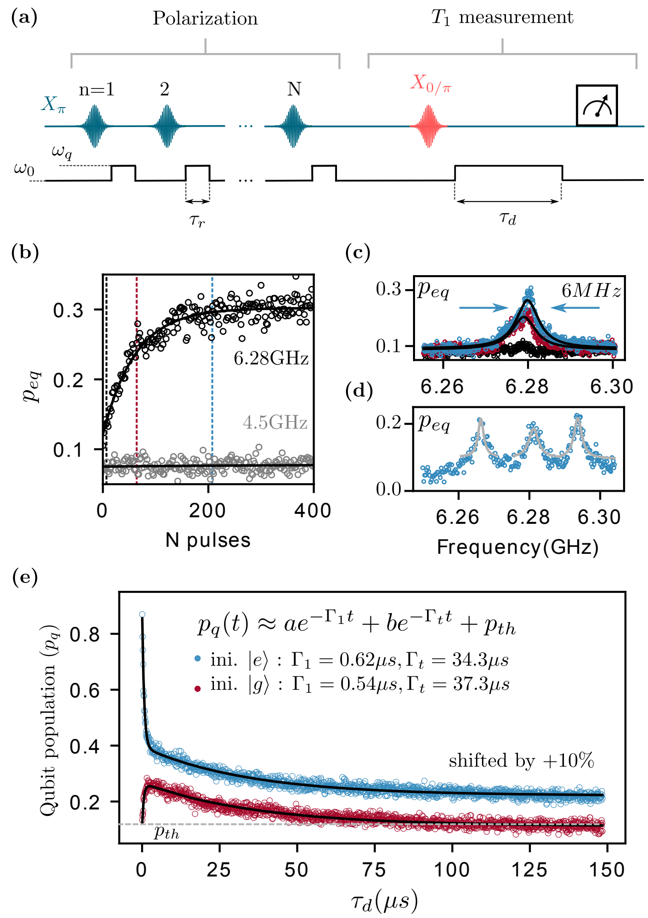

FIG. 2. **Polarization of two-level systems (TLSs).** (a) Pulse sequence of TLS polarization and population measurement. The qubit is prepared in the excited state at $\omega_0/2\pi = 6.3$ GHz and is allowed to decay at ω_q by waiting for $\tau_r = 1\,\mu$s $> 1/\Gamma_1$. After the sequence is repeated N times, the qubit is prepared either in the $|g\rangle$ or $|e\rangle$ state, and T_1 measurement is performed at ω_q. The equilibrium population $p_{eq} \approx p_q(\tau_d = 5\mu s)$ as a (b) function of pulse number N inside (black) and outside (gray) the phononic bandgap, and (c) as a function of frequency around 6.28 GHz for $N = 0, 50, 200$. The 6 MHz linewidth of the saturated bath indicates a high density of weakly coupled TLSs. (d) Spectral bath saturation at three adjacent frequencies using interleaved polarization pulses. (e) Measured relaxation of the qubit after 200 polarization pulses at 6.28 GHz followed by qubit initialization in the $|g\rangle$ (red) and $|e\rangle$ state (blue). The decay rate is biexponential with fast/slow decay components that correspond to the qubit/TLS lifetimes respectively, as detailed in the inset equation and fitted parameters.

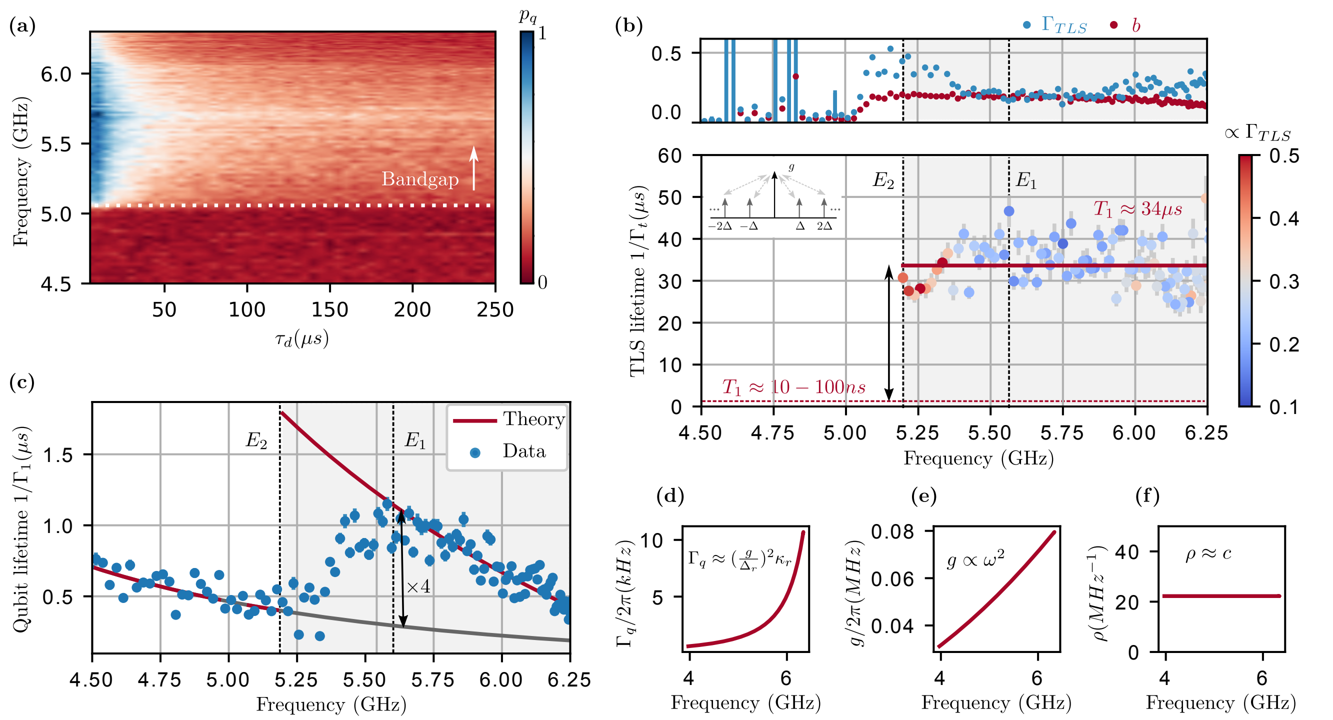

FIG. 3. **Phononic bandgap spectrsocpy.** (a) Qubit population spectroscopy after N polarization pulses showing a clear transition at the phononic bandgap edge (5.2 GHz). (b) and (c) are the qubit ($1/\Gamma_1$) and TLS ($1/\Gamma_t$) lifetimes extracted by fitting to the biexponential function $p_q(t) \approx ae^{-\Gamma_1 t} + be^{-\Gamma_t t} + p_{th}$. The TLS lifetime increases to an average of 34 μs inside the phononic bandgap, corresponding to a 4-fold improvement in the qubit lifetime. The signature of the bandgap structure can be traced by examining $b \propto \Gamma_{TLS}/\Gamma_1$, which is plotted on the top part of (b) as well by coloring the TLS lifetime. Γ_{TLS} increases when moving from E_1 to E_2, which corresponds to the band edges of the Si and Si/Al unit cell, respectively, as was illustrated in Fig. 1 (c). From the decay rates data, and using Eq. 1 we plot the fitted intrinsic qubit decay Γ_q (Purcell-limited by the readout resonator), the coupling strength g ($\propto \omega^2$), and the TLS density ρ (constant) in (d), (e), and (f), respectively. The model assumes constant coupling g and periodic TLS arrangement as illustrated in the inset of (b). The fitting diverges in the frequency range between E_1 and E_2 as a subset of the TLSs leaves the bandgap.

Fig. 3(b) and (c), respectively. The phononic bandgap improves the TLS lifetime to an average of 34 µs. The qubit lifetime shows frequency dependence with a modest improvement of up to 4-fold. The smooth 400 MHz transition in the qubit lifetime between E_1 =5.2 GHz and E_2 =5.6 GHz corresponds to the difference in the band edge frequency between the Si and Si/Al phononic crystal unit cells, respectively, as illustrated in Fig. 1(c). The signature can also be captured by examining the qubit decay due to the coupled TLSs (Γ_{TLS}), which can be estimated by noting that $b \propto \Gamma_{TLS}/\Gamma_1$ [24]. Γ_{TLS} increases below E_1 as a subset of the TLSs leaves their local phononic bandgap, whereas the fitting diverges completely below E_2, where the majority of TLSs are short-lived, and their lifetime can't be captured by the pulsing sequence. Their lifetime typically falls in the range of 10–100 ns, as reported in [26, 27].

To gain more insight into the TLS bath properties, we fitted the measured qubit lifetimes to the qubit-decay formula (Eq. 1). We simplify the TLS lifetime into a piecewise function of 34 μs for ω >5.2 GHz and 100 ns otherwise. The model also assumes that the TLSs are periodically arranged at a constant density $\rho = 2\pi/\Delta$ and a single coupling strength g (inset of Fig. 3(b)). The sum of this distribution can be found analytically [19] and is detailed in the supplementary information section [24]. The fitted qubit intrinsic decay Γ_q, coupling strength g, and TLS density ρ are extracted and plotted as functions of frequency in Fig. 3(d), (e), and (f), respectively. The extracted intrinsic qubit decay is dominated by the Purcell decay of the readout resonator with a resonance frequency of $\omega_r/2\pi$ =7.1 GHz, a decay rate of $\kappa/2\pi$ =2 MHz, and a qubit coupling strength of $g_q/2\pi$ =48 MHz, which is in good agreement with the measured qubit system (see [24]). The average qubit-TLS coupling strength spans a range of 0.03–0.08 MHz, in good agreement with the electrostatic simulation, where $g = pE$, and p was assumed to be 0.2 eÅ (provided in [24]). However, the frequency dependence is quadratic $\propto \omega^2$ instead of the expected $\propto \sqrt{\omega}$. One possible reason for the disagreement is the oversimplification of the model, where, in practice, g is a complex distribution of space and frequency. Finally, the density of TLS per unity frequency ρ is around 23 MHz^{-1} and approximately constant, as expected from the standard tunneling model [9]. The fitting diverges around the band edge, particularly between E_1 and E_2, where a large subset of TLS leaves their local bandgap range.

Discussion and outlook. The results of this work endorse the piezoelectric picture of TLSs and demonstrate that the phonon relaxation rate can be enhanced or suppressed by engineering the density of states of the immediate environment. By utilizing a full bandgap phononic crystal, the relaxation time of an ensemble of TLSs increased from 10–100 ns to an average of 34 μs. We anticipate that implementing a design with a larger phononic bandgap can further improve the TLS lifetime, potentially extending it to a few milliseconds [28].

The vital aspect of TLS lifetime enhancement is its influence on qubit coherence, which is governed by Eq. 1. The limited four-fold improvement in qubit lifetime (Fig. 3(c)) results from the large density of interacting TLSs formed by the excessive etching of the phononic crystal. This issue can potentially be mitigated by using an epitaxial phononic superlattice with reduced surface defects and structural damage [29]. To clarify, we have plotted in Fig. 4 the analytical sum of the qubit relaxation rate due to an ensemble of TLSs (Γ_{TLS}) with a constant density ρ and equal coupling strength g (provided in [24]). The TLS relaxation rate (Γ_t) varies along one axis, while the other axis assumes that the coupling strength is inversely proportional to the density of TLSs ($g = 1/\rho$). The latter proportionality is qualitatively correct, assuming a constant density of TLSs per unit volume. Therefore, miniaturizing the qubit enhances the coupling strength to a smaller number of TLSs. The color map qualitatively shows two different regimes. When the density of TLS is very large, the TLS relaxation rate does not have much influence, and the qubit decay rate follows that of the Fermi golden rule, $\Gamma_{TLS} \propto g^2\rho$. Modern qubits operate in this regime and mitigate TLS loss by using large planar geometries and cleaner fabrication processes [30, 31]. As the device becomes smaller, decoherence increases significantly due to the strong coupling to short-lived TLSs despite their reduced density, which is the primary bottleneck preventing qubit scaling. The decay rate follows the Purcell formula, $\Gamma_{TLS} \propto (g/\Delta)^2\Gamma_t$, which is directly proportional to the TLS relaxation rate. In this regime, phononic shielding is effective in significantly reducing Γ_t and, therefore, the qubit loss due to TLSs (Γ_{TLS}). This is a promising path toward scaling qubits without significant degradation in their decoherence, a vital step toward practical and sophisticated quantum systems.

Finally, the work demonstrated that the Solomon's equations and the polarization pulse sequences are powerful tools for characterizing an ensemble of incoherent TLSs and can be used to study advanced non-Markovian phenomena such as superradiance and state revivals [32, 33].

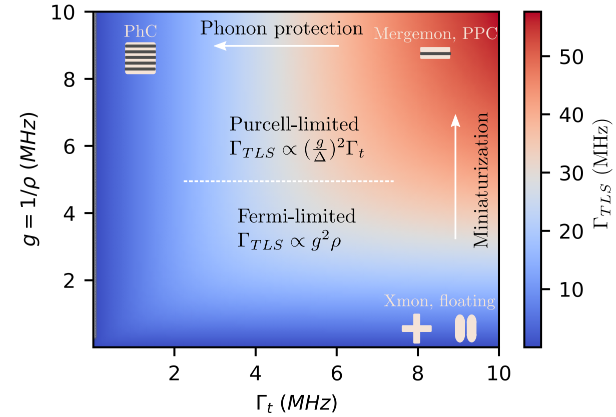

FIG. 4. **Qubit-TLS interaction regimes.** The qubit relaxation rate due to TLSs (Γ_{TLS}), calculated using the analytical sum of Eq. 1 and assuming $\Gamma_q = 0$ and $g = 1/\rho$ [24]. As the qubit size decreases, the relaxation rate transitions from being Fermi-limited (independent of Γ_t) to being Purcell-limited (proportional to Γ_t) due to the reduced density but strengthened coupling of TLSs. Suppressing TLS relaxation using phononic shields becomes vital in preserving qubit coherence, enabling the development of complex, scalable quantum systems.

Acknowledgments. in Quantum Information Science under Award Number DE-SC0022289 for materials processing and first principles modeling, and the NSF hank UC Berkeley, LBNL, Ming Wu and Eli Yablonovitch for their support during the ramp up of our new lab, Quantum Opus for custom SNSPD installation, Auden Young, Andrew Kim, and Xudong Li for technical assistance, and Zihuai Zhang for feedback on the manuscript. The devices used in this work were fabricated at UC Berkeley's NanoLab. the open-source python packages QICK was used in measurment and SCQubit for design, and GDSpy for gds generation.

Appendix A: Analytical modeling

In this section, we review the Solomon equations, which are rate equations that link the qubit population (central spin) to the population of a discrete ensemble of two-level systems (spin environment). We focus on the limit of weakly coupled TLSs that are dense and much longer-lived than the qubit ($\Gamma_t \ll \Gamma_q$). Next, we review the limit of the cross-relaxation rate under a periodic arrangement of the TLSs and constant coupling, illustrating the Purcell-limited and Fermi-limited regimes described in the text. The full and detailed development can be found in [18, 19].

1. The Solomon rate equations

The system is modeled assuming the qubit with population p_q is coupled to a countable number of TLSs with populations p_t^k. We denote Γ_q and Γ_t^k as the intrinsic relaxation rates of the qubit and the kth TLS, respectively. The cross-relaxation rate Γ_{qt}^k is given by

$$\Gamma_{qt}^k = \frac{2g^2\Gamma_2}{\Gamma_2^2 + \Delta_k^2}, \tag{A1}$$

where Δ_k is the detuning between the qubit and the kth TLS, g represents their transverse coupling strength, and mutual decoherence is described by $\Gamma_2 = \Gamma_2^q + \Gamma_2^{t,k}$, with $\Gamma_2 = \Gamma_1/2$ in the absence of dephasing. In the limit where the mutual decoherence of the qubit and TLS is sufficiently strong ($\Gamma_2^k > 4g_k$), the interaction is incoherent, and the population dynamics are governed by the Solomon equations:

$$\dot{p}_q = -\Gamma_q(p_q - p_{th}) - \sum_k \Gamma_{qt}^k(p_q - p_t^k) \tag{A2}$$

$$\dot{p}_t = -\Gamma_t(p_t^k - p_{th}) - \Gamma_{qt}^k(p_t^k - p_q) \tag{A3}$$

From the initial conditions, one can determine the upward and downward transition rates of the qubit

$$\Gamma_\uparrow(t) = \dot{p}_q(t)|_{p_q=0} \text{ and } \Gamma_\downarrow(t) = -\dot{p}_q(t)|_{p_q=q}, \tag{A4}$$

from which, the qubit decay rate and its equilibrium population can be determined

$$\Gamma_1 = \Gamma_\uparrow(t) + \Gamma_\downarrow(t) = \Gamma_q + \sum_k \Gamma_{qt}^k \tag{A5}$$

$$p_{eq}(t) = \frac{\Gamma_\uparrow(t)}{\Gamma_1} = \frac{\Gamma_q p_{th} + \sum_k \Gamma_{qt}^k p_t^k(t)}{\Gamma_1}. \tag{A6}$$

In the special case of identical cross-relaxation rates ($\Gamma_{qt}^k = \Gamma_{qt}$) with a large number of TLSs, the qubit population exhibits biexponential decay behavior.

$$\dot{p}_q = -\Gamma_1(p_q - p_{th}) + \Gamma_{TLS} p_{t,0}^* e^{-\Gamma_t t}, \tag{A7}$$

where $\Gamma_{TLS} = \sum_k \Gamma_{qt}^k$ is the sum of the cross-relaxation rates. It can be shown that in the case of long-lived TLSs ($\Gamma_t \ll \Gamma_1$), an approximate solution to the above differential equation is a biexponential with fast and slow decay parts that encode the qubit and TLS relaxation rates, respectively. The slowly varying amplitude of population decay for the TLSs can be obtained by setting $\dot{p}_q = 0$ (adiabatic elimination), from which the approximate solution to Eq. A7 can be obtained:

$$\boxed{p_q(t) \approx p_{q,0}^* e^{-\Gamma_1 t} + \frac{\Gamma_{TLS}}{\Gamma_1} p_{t,0}^* e^{-\Gamma_t t} + p_{th}} \tag{A8}$$

2. Cross-relaxation rate of periodic TLSs

When the TLSs are spread in frequency and equally spaced by a period Δ with a single coupling strength g and mutual decoherence rate Γ_2, an analytical expression for the cross-relaxation rate can be obtained as follow:

$$\Gamma_{TLS} = \sum_k \frac{2g^2\Gamma_2}{\Gamma_2^2 + \Delta_k^2} \tag{A9}$$

$$= \sum_{h=-\infty}^{\infty} \frac{ab^2}{b^2 + (h - bc)^2} \tag{A10}$$

$$\Gamma_{TLS} = \pi ab \frac{\sinh(2\pi b)}{\cosh(2\pi b) - \cos(2\pi bc)} \tag{A11}$$

where $a = 2g^2/\Gamma_2$, $b = \Gamma_2/\Delta$, $c = \Delta_0/\Gamma_2$ with Δ_0 being the shift of the periodic TLS with respect to the qubit and can take any value between $\Delta_0 \in \{0, \Delta/2\}$. In the limit of sparse TLSs ($b \to 0$), the sum can be terminated to the few nearest interacting TLSs, and the decoherence follows the Purcell formula $\Gamma_{TLS} \approx (g/\Delta)^2\Gamma_t$. In the limit of dense TLSs ($b \to \infty$), Eq. A11 is approximately equal to πab and $\Gamma_{TLS} \approx 2\pi g^2\rho$ which is the Fermi's golden rule and is independent of the TLS relaxation time.

Appendix B: Qubit parameters and coherence properties

We report the measured parameters as follows: $\omega_q/2\pi$ =6.3 GHz, $\alpha/2\pi$= −180 MHz, $\omega_r/2\pi$ =7.06 GHz, $\Lambda/2\pi$ =4 MHz, and $\chi/2\pi$ = 1 MHz. Here, $\alpha = \omega_{21} - \omega_{10}$ represents the anharmonicity which is inferred from the two-photon excitation (Fig. S1 (a)), ω_r is the readout resonator frequency, $2\chi = \omega_{r,|0\rangle} - \omega_{r,|1\rangle}$ denotes the dispersive shift, and $\Lambda = g^2/\Delta$ represents the Lamb shift. These measured values imply a Josephson energy $E_J/\hbar$ = 30 GHz in the transmon limit ($E_J \gg E_C$), where $\hbar\omega_q \approx \sqrt{8E_JE_C} - E_C$, and a charging energy $E_C \approx -\hbar\alpha$. The readout-qubit coupling is $g/2\pi$ = 55 MHz, where $g \approx \sqrt{-\Delta\chi(1 + \Delta/\alpha)}$, and the detuning is $\Delta = \omega_q - \omega_r$. The readout resonator has an extrinsic quality factor of $Q_e = 3.7k$ and an intrinsic quality factor $Q_i = 0.14 - 1.7 \times 10^5$ that range from the single photon limit to the power-saturated limit.

At $\omega_q/2\pi$ =6.3 GHz, we measure a relaxation time $T_1 = 0.42$ µs and Ramsey dephasing time $T_2^* = 0.61$ µs, as shown in Fig. S1(b) and (c), respectively. The qubit can be tuned continuously from 6.3–4 GHz with no signatures of swapping or splitting, suggesting incoherent interaction with the TLS environment (Fig. S1(d)). We note that the Purcell decay through the readout resonator is below 1/13 µs^{-1} and does not limit our coherence measurements. Finally, the qubit population measurements presented in the manuscript are normalized to the fitted readout amplitude distribution when the qubit is prepared in the ground (blue) and excited (red) states, respectively, as shown in Fig. S1(e).

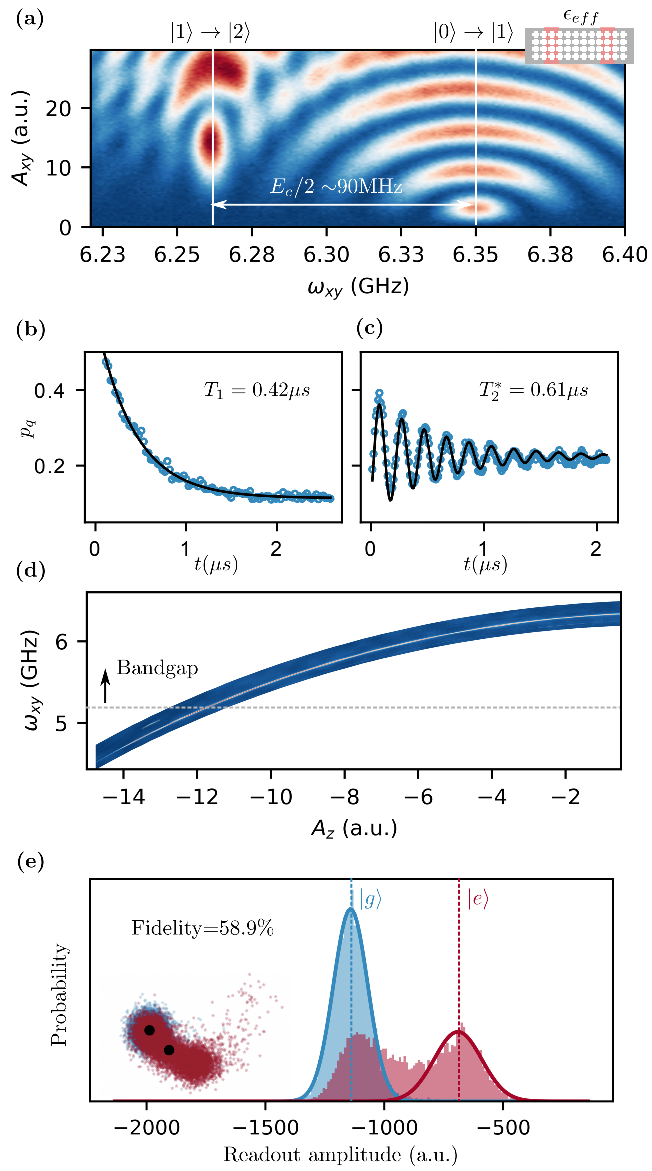

FIG. S1. **Coherence properties of the qubit.** (a) Excited and high-order state populations of the transmon as functions of the XY drive frequency and amplitude, from which the qubit capacitance can be estimated as $E_c/2 \approx e^2/4C_q$. (b) Qubit relaxation time $T_1 = 0.42\,\mu\text{s}$ and (c) Ramsey dephasing $T_2^* = 0.61\,\mu\text{s}$ times measured at the flux-insensitive point ($\omega_q = 6.3\,\text{GHz}$). The relaxation time after each measurement was set to $200\,\mu\text{s}$ to ensure that the long-lived TLS bath relaxes to its thermal equilibrium. (d) Qubit two-tone spectroscopy showing a smoothly varying curve inside and outside the phononic bandgap. The absence of avoided level crossings indicates incoherent interaction with weakly coupled TLS bath. (e) Probability of the readout resonator amplitude for a single-shot measurement of the qubit state in the ground (blue) and excited (red) states. The readout fidelity is 58.9% and is limited by the qubit relaxation time and the inset shows the IQ blob measurement.

Appendix C: Electrostatic simulation

The vast scale difference between the phononic wavelength and the total capacitance dimensions posed a problem in estimating the qubit capacitance via electrostatic simulation and the qubit coupling to the readout resonator. We resorted to finding the effective medium permittivity representation of the phononic crystal for a test structure and found that the capacitance is equivalent if the silicon slab substrate is substituted with a flat one with $\epsilon_{eff} = 3.5$, assuming that most of the electric field is planar, as illustrated in Fig. S2 (a). The results are in good agreement with the experiment and simulation of the IDC under periodic boundary conditions.

To verify the coupling strength extracted in the experiment, we simulated two different occurring cross-sections of the IDC: one with a silicon layer of 190nm that extends through the bridges and the thickness, and the other with vacuum, ignoring it. From the qubit measurement parameters, we set the voltage between the two electrodes to $V_{zpf} = 4\,\mu\text{V}$, which was estimated from the measured qubit parameters through $V_{zpf} = \omega\sqrt{\hbar Z_T/2}$, where the transmon impedance is $Z_T = (\Phi_0/\pi e)\sqrt{E_C/2E_J}$. The coupling strength g is on a $3\,\text{nm}$ thick layer.

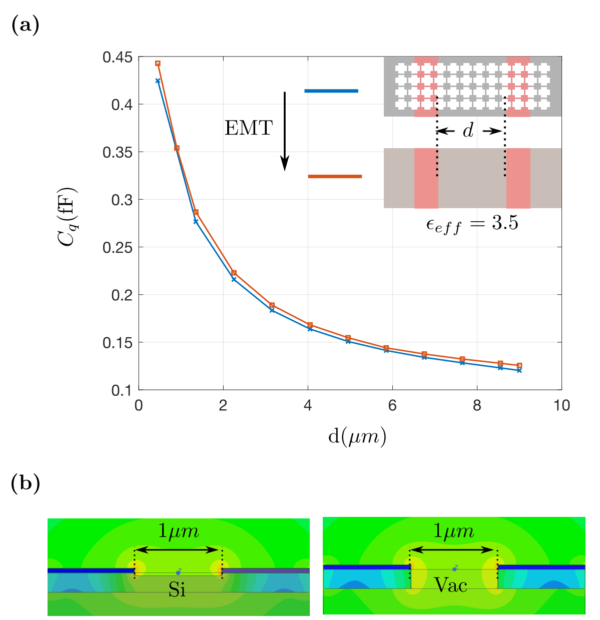

average $g/2\pi$(MHz) for $p = 0.2e\mathring{A}$ & $V_{zpf} = 4\mu V$			
Gap	SV	SM	MV
Si	0.29	0.08	0.02
Vac	0.08	0.03	0.02
W. Avg.	0.11	0.04	0.02

FIG. S2. Schematic of the fabrication steps for phonon protected superconducting qubit and detailed in the text.

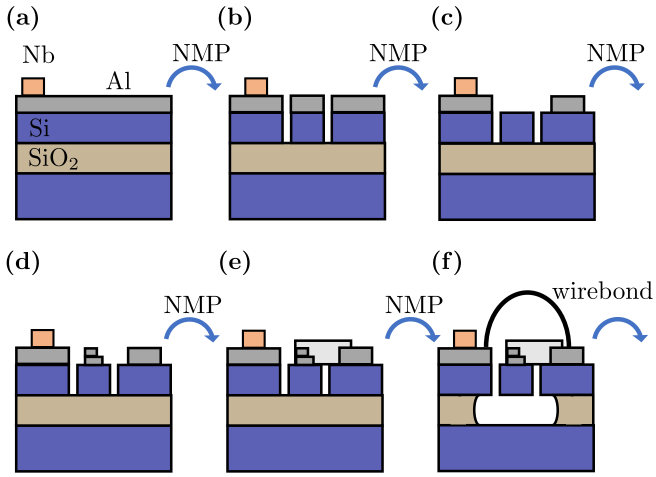

FIG. S3. Schematic of the fabrication steps for the phonon-protected superconducting qubit: (a) Nb alignment marks; (b) phononic crystal electron beam lithography (EBL) and dry etching; (c) microwave circuit EBL and dry etching; (d) Josephson junction EBL and liftoff; (e) bandage EBL and liftoff; and (f) airbridges followed by vapor HF device release.

Appendix D: Device fabrication

In this section, we provide the detailed fabrication process flow for the phonon-protected transmon qubit (Fig. S3), which is a variation of the process presented in [34]. The SOI wafer used (supplied by Shin-Etsu) features a float zone silicon device layer with a thickness of 220 nm and a crystal orientation of 100 ($\rho \geq 3\,\mathrm{k}\Omega\,\mathrm{cm}$). The BOX is a 3 µm-thick layer of SiO_2 on top of a Czochralski-grown silicon handle layer with a thickness of 725 µm ($\rho \geq 3\,\mathrm{k}\Omega\,\mathrm{cm}$).The wafer, protected with a resist coating, is downsized from 8″ to 6″ (by MicroPE). Before deposition, the wafer is cleansed with H_2SO_4 and H_2O_2 (piranha solution) to remove organic residues, dipped in HCL to remove metallic contamination, and then in HF to remove the native oxide. Next, 50 nm of aluminum is sputtered at a rate of 15 nm/min. Since the contrast between materials with similar atomic numbers is poor under electron microscopy, and considering that the atomic masses of Si and Al are 28 U and 27 U, respectively, Nb metal (93 U) is used for subsequent electron-beam lithography (EBL) alignments. To define the markers, a 1 μm-thick AZ-MIR 701 resist is exposed (Heidelberg MLA150), developed in MF-26A, and then descummed in O_2 plasma. Next, a 200 nm-thick Nb layer is sputtered at a rate of 28 nm/min, followed by an 1165 lift-off process. The wafer is then protected with resist and diced into 10×10 mm dies for device processing.

The phononic crystal and release holes are then defined. Given the significant membrane size, proximity effect correction (PEC) was set up through BEAMER to address dose distortion. The pattern is subsequently exposed onto 200 nm CSAR resist in an EBL step. The resist is cold-developed in AR600-546, and the pattern is transferred through two consecutive dry etching steps: a 50 nm aluminum etch using a Cl_2/BCl_3 chemistry, followed by a 220 nm silicon etch using $Cl_2/HBr/O_2$ chemistry. The addition of O_2 helps preserve the aluminum thin bridges and corners from being thinned and rounded during the silicon etch. The sample is immediately immersed in water to passivate the chlorinated aluminum, followed by resist stripping in 80 °C 1165 remover for 30 min.

Next, the microwave circuit is defined by patterning 400 nm PMMA A6 resist in an EBL step. To mitigate stitching errors, a 10 μm field overlap is employed, along with a 2-multipass exposure configured using BEAMER. The resist is developed in MBIK/IPA at a 1:3 ratio, and the pattern is transferred by dry etching 50 nm of Al and 30 nm of Si. The silicon over-etching improves the surface for the Josephson junction evaporation. The sample is once again treated with water to passivate the chlorinated aluminum, and the resist is stripped by a 30 min soak in 80 °C 1165 remover.

The Josephson junctions are defined through EBL exposure of a 400 nm/200 nm EL9/CSAR bilayer resist. The exposed resist is then sequentially cold-developed (MBIK-IPA 1:3/AR600-546) and gently descummed in O_2 plasma. The sample is loaded into a double-angle evaporator (Plassys MEB550) and pumped down to a base pressure of 4×10^{-8} mtorr with the assistance of Ti guttering. The subsequent steps are carried out in the following order: a 30 nm Al evaporation at coordinates ($\theta = 45$, $\phi = 45$); dynamic oxidation at 20 mbar for 20 min; another 30 nm Al evaporation at ($\theta = 45$, $\phi = -90$); and a 40 nm Al evaporation at ($\theta = 45$, $\phi = 90$). The evaporation during all these steps is conducted at a rate of 0.3 nm/sec. The liftoff process is carried out by soaking the sample for 2 h in a 50 °C Acetone bath, followed by a 30 min soak in 80 °C 1165 remover.

A second EBL step was employed to define a bandage layer. An ion milling process was used to remove the native oxide layer from the Al, followed by an Al evaporation step at ($\theta = 0, \phi = 0$), conducted at a rate of 1 nm/sec, resulting in a thickness of 200 nm. A liftoff and cleaning process similar to the one used in the JJ step was carried out. This step also served to increase the Z-line CPW thickness from 50 nm to 250 nm, allowing for a larger current capacity and avoiding heating issues. Aluminum wire bonds were used as airbridges to mitigate slot-line modes, which happen to be at lower frequencies than the main mode in released SOI CPW resonators. This step precedes the releasing process as wire bonding near suspended devices may induce structural collapse. The device is released using vapor HF through a 4 µm isotropic oxide etch, conducted at a rate of 36 nm/min. Finally, the sample is mounted and wire-bonded onto a PCB enclosed by a copper box for measurement.

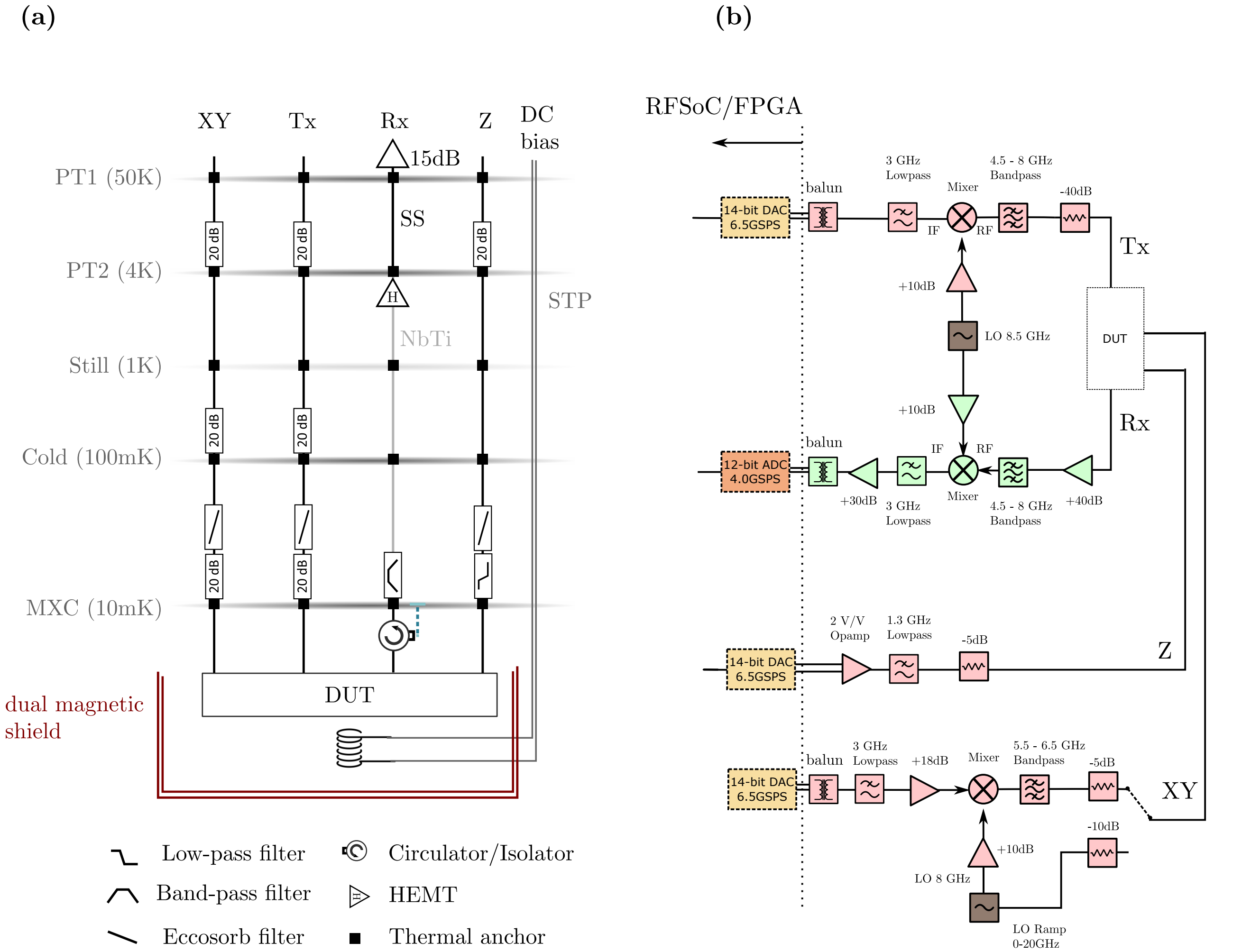

FIG. S4. Experimental setup schematics for (a) dilution refrigerator cryogenic wiring, and (b) room temperature microwave electronics.

Appendix E: Cryogenic setup and microwave electronics

We characterize the qubit in a ^{3}He$-^4$He dry dilution refrigerator (Bluefors, BF-LD250). This refrigerator comprises multiple temperature stages, namely PT1, PT2, Still flange, cold plate (CP), and mixing chamber (MXC) flange, as illustrated in Fig. S4(a). The Tx and Rx lines are used to probe the readout resonator, the XY line for qubit control, and the Z/DC-bias lines for dynamic/static control of the qubit's frequency. The Tx, XY, and Z lines pass through a series of cryogenic attenuators with a total of 60 dB/60 dB/20 dB attenuation, respectively [35]. All the input lines are filtered with Eccosorb IR filters (QMC-CRYOIRF-002MF-S), and an additional low-pass filter is added to the Z line (Minicircuits VLFX-1300+). The return Rx line passes through 44 dB of isolation (2 x LNF-CIC4 8A), a bandpass filter (Keenlion KBF-4/8-2S), and is connected to a 42 dB HEMT amplifier (LNF-LNC4 8C) through NbTi superconducting RF cable. The sample is mounted vertically inside a dual-cylinder magnetic shield (Cryo-Netic) along with an aligned superconducting coil made from NbTi DC wire for static biasing.

We use a Zynq UltraScale+ RFSoC board with the QICK (Quantum Instrumentation Control Kit) FPGA overlay for coherent RF signaling and acquisition up to 3 GHz frequency [36]. Front-end heterodyne stages with external local oscillators (LMX2595) parked at 8.5 GHz/8 GHz for the Tx/XY lines are used for signal up-conversion to the desired readout/qubit frequency. For the Z-line, we employ a DC to 800 MHz Differential-to-Single-Ended Opamp with a 5000 V μs^{-1} slew rate for fast qubit tuning (TI THS3217), followed by a 1.3 GHz low-pass filter (MC VLFX-1300). A series of amplifiers, filters, and attenuators are employed across the entire chains to ensure proper frequency mixing, sideband suppression, and utilization of the full DAC/ADC range, as illustrated in Fig. S4(b).

[1] P. W. Shor, Scheme for reducing decoherence in quantum computer memory, Phys. Rev. A **52**, R2493 (1995).
[2] A. G. Fowler, M. Mariantoni, J. M. Martinis, and A. N. Cleland, Surface codes: Towards practical large-scale quantum computation, Phys. Rev. A **86**, 032324 (2012).
[3] E. Knill, R. Laflamme, and W. H. Zurek, Resilient quantum computation: error models and thresholds, Proceedings of the Royal Society of London. Series A: Mathematical, Physical and Engineering Sciences **454**, 365 (1998).
[4] G. Q. AI, Suppressing quantum errors by scaling a surface code logical qubit, Nature **614**, 676 (2023).
[5] A. D. Córcoles, E. Magesan, S. J. Srinivasan, A. W. Cross, M. Steffen, J. M. Gambetta, and J. M. Chow, Demonstration of a quantum error detection code using a square lattice of four superconducting qubits, Nature Communications **6**, 6979 (2015).
[6] P. W. Shor, Polynomial-time algorithms for prime factorization and discrete logarithms on a quantum computer, SIAM Journal on Computing **26**, 1484 (1997).
[7] L. K. Grover, A fast quantum mechanical algorithm for database search, in *Proceedings of the Twenty-Eighth Annual ACM Symposium on Theory of Computing*, STOC '96 (Association for Computing Machinery, New York, NY, USA, 1996) pp. 212–219.
[8] J. O'Gorman and E. T. Campbell, Quantum computation with realistic magic-state factories, Phys. Rev. A **95**, 032338 (2017).
[9] C. Müller, J. H. Cole, and J. Lisenfeld, Towards understanding two-level-systems in amorphous solids: insights from quantum circuits, Reports on Progress in Physics **82**, 124501 (2019).
[10] P. Esquinazi, ed., *Tunneling Systems in Amorphous and Crystalline Solids* (Springer Berlin Heidelberg, 1998).
[11] J. Jäckle, On the ultrasonic attenuation in glasses at low temperatures, Zeitschrift für Physik A Hadrons and nuclei **257**, 212 (1972).
[12] I. Siddiqi, Engineering high-coherence superconducting qubits, Nature Reviews Materials **6**, 875 (2021).
[13] S. Kono, J. Pan, M. Chegnizadeh, X. Wang, A. Youssefi, M. Scigliuzzo, and T. J. Kippenberg, Mechanically induced correlated errors on superconducting qubits with relaxation times exceeding 0.4 milliseconds (2023), arXiv:2305.02591 [quant-ph].
[14] A. P. M. Place, L. V. H. Rodgers, P. Mundada, B. M. Smitham, M. Fitzpatrick, Z. Leng, A. Premkumar, J. Bryon, A. Vrajitoarea, S. Sussman, G. Cheng, T. Madhavan, H. K. Babla, X. H. Le, Y. Gang, B. Jäck, A. Gyenis, N. Yao, R. J. Cava, N. P. de Leon, and A. A. Houck, New material platform for superconducting transmon qubits with coherence times exceeding 0.3 milliseconds, Nature Communications **12**, 1779 (2021).
[15] C. Wang, X. Li, H. Xu, Z. Li, J. Wang, Z. Yang, Z. Mi, X. Liang, T. Su, C. Yang, G. Wang, W. Wang, Y. Li, M. Chen, C. Li, K. Linghu, J. Han, Y. Zhang, Y. Feng, Y. Song, T. Ma, J. Zhang, R. Wang, P. Zhao, W. Liu, G. Xue, Y. Jin, and H. Yu, Towards practical quantum computers: transmon qubit with a lifetime approaching 0.5 milliseconds, npj Quantum Information **8**, 3 (2022).
[16] G. Andersson, A. L. O. Bilobran, M. Scigliuzzo, M. M. de Lima, J. H. Cole, and P. Delsing, Acoustic spectral hole-burning in a two-level system ensemble, npj Quantum Information **7**, 15 (2021).
[17] N. Kirsh, E. Svetitsky, A. L. Burin, M. Schechter, and N. Katz, Revealing the nonlinear response of a tunneling two-level system ensemble using coupled modes, Phys. Rev. Mater. **1**, 012601 (2017).
[18] Two-level system hyperpolarization using a quantum szilard engine, Nature Physics **19**, 1320 (2023).
[19] M. Spiecker, A. I. Pavlov, A. Shnirman, and I. M. Pop, Solomon equations for qubit and two-level systems (2023), arXiv:2307.06900 [quant-ph].
[20] J. Morris, F. A. Pollock, and K. Modi, Quantifying non-markovian memory in a superconducting quantum computer, Open Systems and Information Dynamics **29**, 2250007 (2022).
[21] L. Xiang, Z. Zong, Z. Zhan, Y. Fei, C. Run, Y. Wu, W. Jin, Z. Jia, P. Duan, J. Wu, Y. Yin, and G. Guo, Quantify the non-markovian process with intervening projections in a superconducting processor (2021), arXiv:2105.03333 [quant-ph].
[22] G. Burkard, Non-markovian qubit dynamics in the presence of $1/f$ noise, Phys. Rev. B **79**, 125317 (2009).
[23] Y. J. Rosen, M. A. Horsley, S. E. Harrison, E. T. Holland, A. S. Chang, T. Bond, and J. L. DuBois, Protecting superconducting qubits from phonon mediated decay, Applied Physics Letters **114**, 202601 (2019).
[24] Supplementary Information is available as Appendices.
[25] J. Lisenfeld, A. Bilmes, A. Megrant, R. Barends, J. Kelly, P. Klimov, G. Weiss, J. M. Martinis, and A. V. Ustinov, Electric field spectroscopy of material defects in transmon qubits, npj Quantum Information **5**, 105 (2019).
[26] Y. Shalibo, Y. Rofe, D. Shwa, F. Zeides, M. Neeley, J. M. Martinis, and N. Katz, Lifetime and coherence of two-level defects in a josephson junction, Phys. Rev. Lett. **105**, 177001 (2010).
[27] R. Barends, J. Kelly, A. Megrant, D. Sank, E. Jeffrey, Y. Chen, Y. Yin, B. Chiaro, J. Mutus, C. Neill, P. O'Malley, P. Roushan, J. Wenner, T. C. White, A. N. Cleland, and J. M. Martinis, Coherent josephson qubit suitable for scalable quantum integrated circuits, Phys. Rev. Lett. **111**, 080502 (2013).
[28] M. Chen and O. Painter, Engineering the phonon bath for TLS in a superconducting qubit, in *APS March Meeting Abstracts*, APS Meeting Abstracts, Vol. 2022 (2022) p. Q41.001.
[29] Y. Ezzahri, S. Grauby, J. M. Rampnoux, H. Michel, G. Pernot, W. Claeys, S. Dilhaire, C. Rossignol, G. Zeng, and A. Shakouri, Coherent phonons in si/sge superlattices, Phys. Rev. B **75**, 195309 (2007).
[30] R. Barends, J. Kelly, A. Megrant, D. Sank, E. Jeffrey, Y. Chen, Y. Yin, B. Chiaro, J. Mutus, C. Neill, P. O'Malley, P. Roushan, J. Wenner, T. C. White, A. N. Cleland, and J. M. Martinis, Coherent josephson qubit suitable for scalable quantum integrated circuits, Phys. Rev. Lett. **111**, 080502 (2013).
[31] S. Kono, J. Pan, M. Chegnizadeh, X. Wang, A. Youssefi, M. Scigliuzzo, and T. J. Kippenberg, Mechanically induced correlated errors on superconducting qubits with relaxation times exceeding 0.4 milliseconds (2023), arXiv:2305.02591 [quant-ph].
[32] E. M. Kessler, S. Yelin, M. D. Lukin, J. I. Cirac, and G. Giedke, Optical superradiance from nuclear spin envi-

ronment of single-photon emitters, Phys. Rev. Lett. **104**, 143601 (2010).

[33] S. Dooley, F. McCrossan, D. Harland, M. J. Everitt, and T. P. Spiller, Collapse and revival and cat states with an n-spin system, Phys. Rev. A **87**, 052323 (2013).

[34] A. J. Keller, P. B. Dieterle, M. Fang, B. Berger, J. M. Fink, and O. Painter, Al transmon qubits on silicon-on-insulator for quantum device integration, Applied Physics Letters **111**, 042603 (2017).

[35] S. Krinner, S. Storz, P. Kurpiers, P. Magnard, J. Heinsoo, R. Keller, J. Lütolf, C. Eichler, and A. Wallraff, Engineering cryogenic setups for 100-qubit scale superconducting circuit systems, EPJ Quantum Technology **6**, 2 (2019).

[36] C. Müller, J. H. Cole, and J. Lisenfeld, Towards understanding two-level-systems in amorphous solids: insights from quantum circuits, Reports on Progress in Physics **82**, 124501 (2019).